Magneto-optical microscope magnetometer for simultaneous local probing of magnetic properties

Sug-Bong Choe,[a] Dong-Hyun Kim, Yoon-Chul Cho, Hyuk-Jae Jang, Kwang-Su Ryu, Hae-Seung Lee, and Sung-Chul Shin
Department of Physics and Center for Nanospinics of Spintronic Materials, Korea Advanced Institute of Science and Technology, Taejon 305-701, Korea

(Received 4 January 2002; accepted for publication 7 May 2002)

The design of a magneto-optical microscope magnetometer (MOMM) for simultaneously probing local magnetic properties is described. The MOMM consists of an optical polarizing microscope capable of magneto-optical contrast that is used as a magnetometer by sweeping a magnetic field from an electromagnet. Due to full-field optical imaging, as opposed to single photodiode detection, the system is capable of simultaneous measurement of magnetic hysteresis loops and magnetization viscosity curves on 8000 individual local regions of 400×400 nm^2 area in ferromagnetic materials. The most striking feature of the system is that it provides two-dimensional maps of the local magnetic properties including the coercivity, the switching time, and the activation magnetic moment from two-dimensional arrays of the hysteresis loops and the viscosity curves. We present the local magnetic properties and their correlations in Co/Pd multilayer films prepared by electron-beam evaporation. © *2002 American Institute of Physics.* [DOI: 10.1063/1.1490421]

I. INTRODUCTION

Nowadays, magnetic information technology such as magnetic and magneto-optical recording[1,2] and magnetoelectronic devices[3] plays a key role in the digital information industry. In magnetic information technology, information is stored in the form of magnetic domains in ferromagnetic thin films and the basic process envolved is the reversal of the domains under an applied magnetic field. As the technology rapidly grows to meet the industrial demand for high-density massive data storage, the typical dimension of magnetic information bits continues to shrink below the submicrometer scale. Therefore to achieve high-performance magnetic information technology as well as to develop novel magnetic materials it is imperative to characterize and monitor the dynamic properties of ferromagnetic films and their dependence on the microstructures on a length scale below a micrometer.[4–7]

The characterization of magnetic domain dynamics is also important from a fundamental point of view. Interest has rapidly grown through the experimental observation of the contrasting magnetization reversal dynamics between wall-motion dominant and nucleation dominant processes exhibited in similar samples of many systems.[8–13] Macroscopic magnetic properties are examined to explain the intrinsic origin of the contrasting reversal dynamics based on a micromagnetic consideration of a thermally activated reversal process; it has been well explained that contrasting reversal dynamics could occur among uniform magnetic films of different macroscopic magnetic properties.[13–18] On the other hand, structural irregularity caused by lattice mismatch,[11] interfacial roughness,[19,20] and local structural variation[21,22] have been conjectured to be another origin of the contrasting reversal dynamics. It is very apparent that the domain evolution is microscopically affected by the spatial inhomogeneity of magnetic properties such as coercive force[23] and magnetization.[24] However, a fundamental understanding of their influences requires microscopic studies, including measurements of the microstructural and/or micromagnetic properties, and real-time observation of the evolution of domain structure in a magnetic field. Both experiments need to be carried out on identical microscopic areas of a sample. Quantitative correlations between local coercivity and magnetization reversal dynamics were very recently reported.[25–27]

Versatile experimental techniques including magnetic force microscopy (MFM),[28] near-field scanning optical microscopy (NSOM),[29] scanning electron microscopy with polarization analysis (SEMPA),[30] spin-polarized scanning tunneling microscopy (SPSTM),[31] spin-polarized low-energy electron microscopy (SPLEEM),[32] x-ray magnetic circular dichroism photoemission electron microscopy (XMCD-PEEM),[33] and magnetic transmission x-ray microscopy (MTXM)[34] have been developed to investigate microscopic domain structures with spatial resolution of some tens of nanometers. But despite the advantage of the high spatial resolution of these techniques, they are not applicable to dynamic studies due to the limitation imposed by applying a magnetic field and/or a slow data acquisition time. On the other hand, the magnetic hysteresis of submicrometer-size magnetic dots has been characterized by means of the magneto-optical Kerr effect, either using a focused laser beam or using an optical microscope equipped with a charge-coupled device (CCD) camera;[5–7] all these investigations have been devoted to improving the local probing capability of individual hysteresis loops on a length scale of a few tenths of micrometers. These measurement techniques focused on the whole area of a film or a single local area of the

[a]Electronic mail: SBChoe@lbl.gov

patterned sample. However, simultaneous local probing of a large area with submicrometer-scale resolution of the dynamics of ferromagnetic thin films has remained a scientific challenge to date.

This study was motivated by a desire to construct an instrument capable of simultaneous magnetic probing on a number of individual local regions, based on the full-field optical imaging technique of a conventional magneto-optical Kerr microscope. Our new instrument, called MOMM from the acronym ''magneto-optical microscope magnetometer,'' provides the unique capability of simultaneously measuring 8000 individual local regions for (1) arrays of the local Kerr hysteresis loops while sweeping the external magnetic field from an electromagnet, as well as (2) arrays of the magnetization viscosity curves during magnetization reversal under a constant applied magnetic field. The simultaneous measurement scheme enables us to avoid measurement errors from different runs as well as the magnetic after effect due to a long measurement time. In addition, the most striking feature of the present system is the fact that one can directly map the local distribution of magnetic properties such as the coercivity, the switching time, and the activation magnetic moment from the arrays of the simultaneous local measurements. In this way, the local variations of the magnetic properties can be directly compared with each other to search for any correlations between them. The ability to do spatially resolved probing of the magnetic properties enables us not only to determine their real distributions, but also to obtain an in-depth understanding of domain reversal dynamics.

In this article, the technical outline is described in Sec. II, and some first results are presented in Sec. III.

II. INSTRUMENTATION DESCRIPTION

The MOMM system is a magnetometric setup of a magneto-optical Kerr microscope, which is a well-established technique extensively used in magnetic domain observation.[6–13,19–25,35–37] The magneto-optical Kerr microscope is basically a polarizing optical microscope that detects magnetic contrast via the magneto-optical Kerr effect, i.e., the rotation of the light polarization angle during reflection at a magnetized specimen. The microscope can visualize the perpendicular component of the magnetization via the polar Kerr effect with a normal incidence of the illumination light, or the longitudinal component of the magnetization via the longitudinal Kerr effect with an inclined incidence of the illumination light by shifting the objective lens and adjusting the relevant optical components. General layouts of the magneto-optical Kerr microscope can be found in the literature.[8,12,13,36,37] Here, we breifly review our microscope setup and then describe the MOMM technique for simultaneous probing of magnetic properties.

The maximum spatial resolution of our optical microscope (Olympus, BX-60M) is about 400 nm at the maximum 1 000× magnification using a 100 W mercury illumination lamp. The mercury lamp is powered via an automatic voltage regulator to enhance the stability. By adopting the sheet-type polarizer/analyzer and a stress-free polarizing objective lens, the Kerr angle resolution in the polar geometry (or bright field illumination) is less than 0.2° for a fast dynamic measurement and 0.01° for a slow, quasi-static measurement.

The system is equipped with an electromagnet controlled by a personal computer to apply an external magnetic field to the sample in the range of ± 3.5 kOe with a field resolution of less than a few tens of Oe. The field rising rate is about 10^{-4} s/Oe with a low-pass filter circuit. We control the electromagnet slower than the field rising rate to avoid an overshooting problem. The electromagnet is positioned just below the sample stage with a gap of about 2 mm. An applied magnetic field from the 6 mm diameter magnetic pole tip is uniform at the sample over a field of view of about 100 μm. The electromagnet is cooled by water to avoid a temperature change of the sample as well as any thermal drift effects of the sample stage. To enhance the stage stability we remove all magnetic materials as well as all rubbers in the micropositioner of the stage. The stage usually settles to a stable position within an hour after sample positioning and then remains stable over a few hours which is enough time to carry out an experiment.

An advanced charge-coupled device (CCD) camera system equipped with a signal intensifier is attached to the microscope to store the magnetic images onto a computer at video rate. The multichannel plate signal intensifier enhances the image intensity by up to 10^4 to image the detailed contrast change from a small Kerr rotation angle usually less than 0.1°. The physical size of a unit CCD pixel is adjusted to correspond to an area of 200×200 nm^2 at the film surface, and we use the sum of a 2×2 pixel array as a logical pixel size Δ to meet the spatial resolution of the microscope; this logical definition of a pixel size will be used from now on. In the current setup a domain image is composed of 100×80 logical CCD pixels. The domain image is then given by an array of the Kerr intensity $I(x,y)$ measured by each position-specified (x,y)th CCD pixel, where x and y are integers.

By storing domain images $I(x,y)$ while sweeping external magnetic field h, one obtains a three-dimensional array of the Kerr intensity $I(x,y;h)$ as depicted in Fig. 1(a), where each pixel contains the position- and field-specified element of the measured Kerr intensity. The cross-sectional mapping onto the (x,y) plane gives the conventional domain images $I_h(x,y)$ at a given field h as shown in Fig. 1(b). However, we would like to point out that tracing along a (x,y) pixel provides a Kerr intensity variation $I_{xy}(h)$ with respect to sweeping an applied field h as shown in Fig. 1(c). The Kerr intensity variation $I_{xy}(h)$ directly correlates to the magnetic hysteresis loop from a local region of Δ^2 area at the (x,y)th position.[27]

Figure 2(a) shows a typical Kerr intensity variation $I_{xy}(h)$. The intensity $I_{xy}(h)$ is correlated with the Kerr rotational angle $\theta_{xy}(h)$ as given by

$$I_{xy}(h)=I_{xy}^{(0)}+C_{xy}\sin^2[\theta_{xy}(h)+\alpha_{xy}h+\delta\theta_{xy}], \tag{1}$$

where $I_{xy}^{(0)}$ is the intensity offset of the corresponding CCD pixel, C_{xy} is the proportional coefficient between the intensity and the Kerr rotational angle, α_{xy} is the Faraday coefficient incurred at the objective lens of the microscope, and $\delta\theta_{xy}$ is the angle between the polarizer and the analyzer. Fitting the measured $I_{xy}(h)$ versus h with Eq. (1) for the two

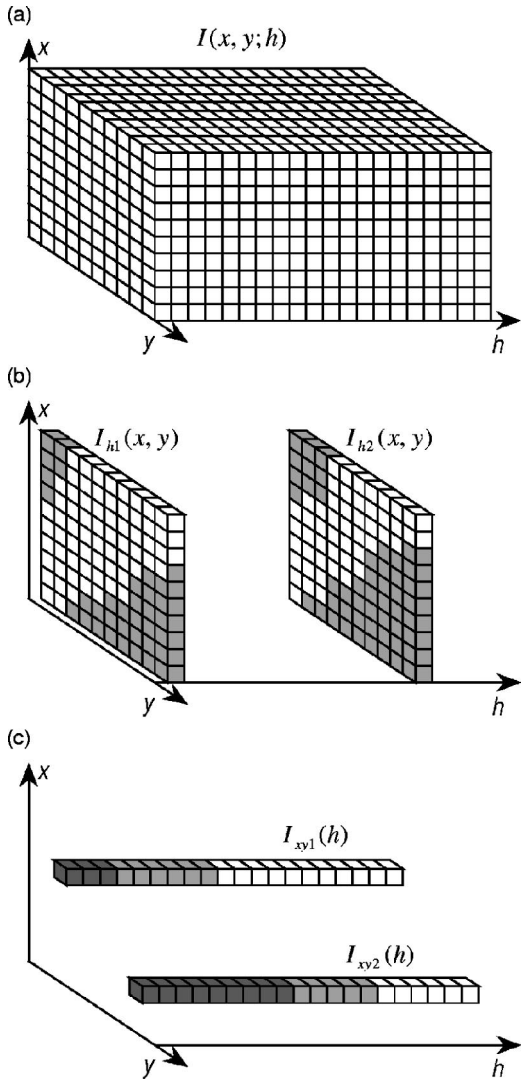

FIG. 1. (a) Schematic representation of a three-dimensional array of position- and field-specified Kerr intensity. (b) Conventional field-dependent domain images, as a cross-sectional view of the three-dimensional array. (c) Field-dependent Kerr intensity variation, at a given CCD pixel.

saturated states of $\theta_{xy}(h)=\pm\theta_{xy}^{\max}$ as shown by the solid lines in Fig. 2(a), one can determine the values of $I_{xy}^{(0)}$, $C_{xy}\alpha_{xy}^2$, $\delta\theta_{xy}/\alpha$, and $\theta_{xy}^{\max}/\alpha$ under an approximation of $\sin\theta\sim\theta$ for a small θ. Then, the normalized Kerr hysteresis loop can be generated from the intensity variation with the fitting quantities by

$$\frac{\theta_{xy}(h)}{\theta_{xy}^{\max}}=\frac{\alpha_{xy}}{\theta_{xy}^{\max}}\left(\sqrt{\frac{I_{xy}(h)-I_{xy}^{(0)}}{C_{xy}\alpha_{xy}^2}}-h\right)-\frac{\delta\theta_{xy}}{\theta_{xy}^{\max}}. \tag{2}$$

Figure 2(b) shows the normalized Kerr hysteresis loop generated from the intensity variation shown in Fig. 2(a). It was confirmed that the measured hysteresis loop of a given local area was basically identical for several different runs. Note that this Kerr hysteresis loop generation process can be simultaneously carried out for every CCD pixel once a three-dimensional array of field-dependent domain images is provided. Thus from the position-specified array of the local hysteresis loops one generates a two-dimensional distribution map of the local coercivity $H_C(x,y)$.

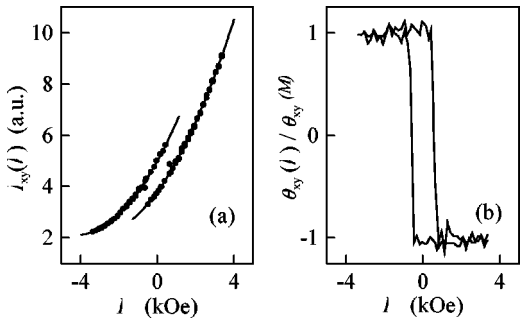

FIG. 2. (a) Typical value of the local intensity variation $I_{xy}(h)$ measured by the (x,y)th CCD pixel as a function of an applied magnetic field H. The solid lines are the fitting curves given by Eq. (1) for the two saturated states of $\theta_{xy}(h)=\pm\theta_{xy}^{\max}$. (b) The normalized Kerr hysteresis loop $\theta_{xy}(h)$ generated from the intensity variation shown in (a).

A similar measurement technique can be applied to measure the local magnetization viscosity curves.[26] In this experiment, a sample is first saturated by applying a magnetic field normal to the film plane and then magnetization reversal is triggered by applying a constant magnetic field h. From the experiment, a three-dimensional array $I(x,y;t)$ is obtained by storing the time-resolved domain images $I(x,y)$ with respect to the elapsed time t during magnetization reversal. Tracing a (x,y) pixel provides the local magnetization viscosity curve $I_{xy}(t)$ as shown in Fig. 3(a) and then one can determine the local magnetization switching time $\tau(x,y)$. From the position-specified array of the local switching time $\tau(x,y)$, one generates a two-dimensional distribution map of the local switching time. On the other hand, if one repeats the $\tau(x,y)$ measurement while changing the applied field h as shown in Fig. 3(b), one can obtain another three-dimensional array of field-dependent $\tau(x,y;h)$, which provides the distribution map of the activation magnetic moment $m_A(x,y)$, as will be discussed in Sec. III. It should be emphasized that all the two-dimensional maps, $H_C(x,y)$, $\tau(x,y)$, and $m_A(x,y)$ are generated from the position-specified arrays; thus the local magnetic properties of each position can be directly compared with each other to search for any correlations among them.

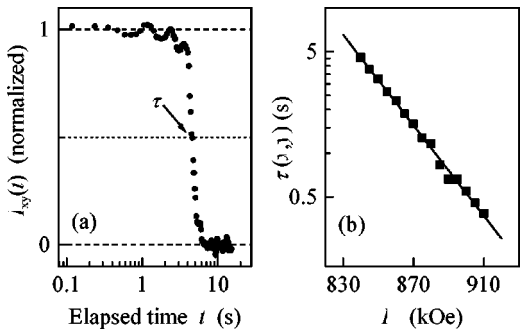

FIG. 3. (a) Typical viscosity curve measured from a CCD pixel corresponding to an area of $0.4\times0.4\ \mu m^2$ at the $(2.5\ \text{Å Co}/11\ \text{Å Pd})_{10}$ sample surface. The y axis is normalized between the Kerr signals from the initially saturated state and the completely reversed state. (b) Field dependence of the magnetization switching time of the given local area. The solid line is the best fit using Eq. (3).

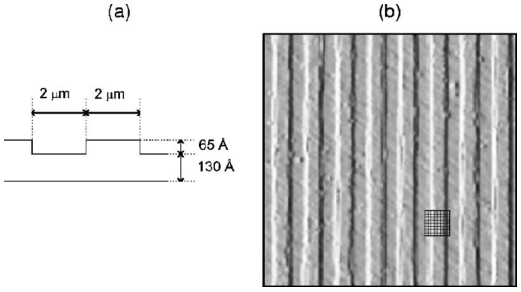

FIG. 4. (a) Schematic cross-sectional view and (b) AFM surface image of a stripe-patterned (2 Å Co/11 Å Pd)$_{15}$ multilayer film.

III. RESULTS AND DISCUSSION

A. Mapping of local magnetic properties

First, we have applied the MOMM to test the sensitivity of magnetic hysteresis variation on a microstructural fluctuation. For this purpose, we have fabricated stripe-patterned (2 Å Co/11 Å Pd)$_{15}$ multilayer films. The samples were prepared on glass substrates by electron-beam evaporation and the stripe patterns of periodic terraces and grooves were realized by photolithography on a photoresist material, followed by the development in a solution and then, an ion milling process. Figure 4 shows (a) a schematic cross-sectional view of the sample and (b) the surface topology of the sample measured by an atomic force microscope (AFM).

By means of the MOMM, we measured the hysteresis loops of each $400\times400\ \mathrm{nm}^2$ local area of the sample. For illustration, a small portion of the local hysteresis loops are depicted in Fig. 5(a), where the measurement area corresponds to the boxes designated in Fig. 4(b). In each hysteresis loop, the x axis is an applied field ranging from -2 to 2 kOe and the y axis is the normalized polar Kerr rotational angle of a perpendicularly magnetized film. Strikingly, it can be clearly observed that the modulation of the local hysteresis loops is closely related with the structural modulation:

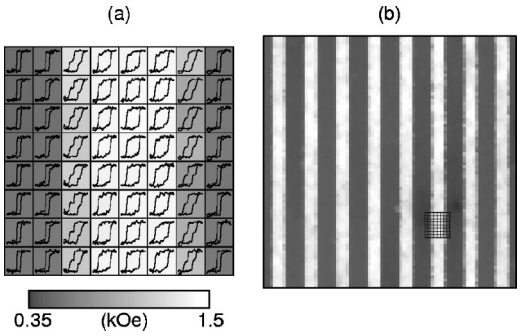

FIG. 5. Generation of a two-dimensional spatial distribution map of the local coercivity variation of a stripe-patterned (2 Å Co/11 Å Pd)$_{15}$ multilayer film, from directly analyzing the local hysteresis loops of every local area simultaneously measured under an identical condition. (a) Measurement of the hysteresis loops for each square pixel of $400\times400\ \mathrm{nm}^2$ located at each corresponding box in Fig. 4, where the x axis is an applied field ranging from -2 to 2 kOe and the y axis is the normalized Kerr rotational angle. (b) The two-dimensional spatial distribution map of the local coercivity variation from the local hysteresis loop measurement, where the measurement area exactly corresponds to Fig. 4. The gray level corresponds to the magnitude of the local coercivity of each corresponding pixel, according to the gray palette at the bottom.

the loops across the pattern are exactly modulating with the structural modulation, even though the loops along the pattern are almost identical. Note that the terrace shows the wide square loops having a large coercivity and the groove shows the narrow square loops having a small coercivity. The contrasting change in the shape of the hysteresis loops is ascribed to the magnetic properties of each region having different thickness, since the coercivity increases with increasing the number of Co/Pd bilayers for this multilayer system.[13] The edge between the two regions shows stepwise loops, which is partially ascribed to the exchange-coupled magnetization reversal dynamics or partially due to the measurement area overlapping between the two regions. For a clear visualization of the local coercivity variation, the gray level filled inside each pixel indicates the magnitude of the coercivity of each corresponding hystersis loop, according to the gray palette at the bottom of the figure.

The most striking feature of the MOMM system is the fact that we can generate the two-dimensional spatial distribution map of the local coercivity variation of a sample by directly analyzing the local hysteresis loops of every local area simultaneously measured under identical conditions. In Fig. 5(b), we illustrate the local coercivity distribution map of a $32\times32\ \mu\mathrm{m}^2$ area of the stripe-patterned sample with a unit pixel of $400\times400\ \mathrm{nm}^2$, where the measurement region is identical with the area shown in Fig. 4(b). One can see a beautiful correlation between the structural modulation and the coercivity variation, where the coercivity is modulated with the exact same periodicity as the structural modulation. To our knowledge, this is the first experimental demonstration that the local structural variation sensitively affects the coercivity. Here, we point out that the experimental capability of local-coercivity probing of magnetic materials is very useful for realistic modeling of magnetization dynamics in both the micromagnetism and the Preisach approach.[23,38,39]

In addition to the major variation across the stripes in Fig. 5, one can notice the minor variation of the coercivity along the stripes, which might be ascribed to the physical- and/or chemical microstructural-irregularities inside the patterns. Since the multilayer films were prepared by electron-beam evaporation under high vacuum conditions, microstructural irregularities in the films naturally exist due to, for example, lattice misfits, residual stress, impurities, and other possible defects created during the sample preparation process.[25] An extremely interesting question is whether the MOMM is sensitive enough to probe the variation of the local dynamic behavior caused by inherently existing microstructural irregularities. For this study, we have prepared (2.5 Å Co/11 Å Pd)$_5$ multilayer films without any artificial structural pattern and thus only with inherent microstructural irregularities.

Using the MOMM, we could indeed probe the variation of the local hysteresis variation as demonstrated in Fig. 6. The typical hysteresis loops of a small portion of the sample area are illustrated in Fig. 6(a), where each loop shows the local hysteresis loop of each corresponding unit area of $400\times400\ \mathrm{nm}^2$. The shape of the hysteresis loops appears to be the same, but a close examination reveals that the value of the coercivity varies slightly. We generated a coercivity dis-

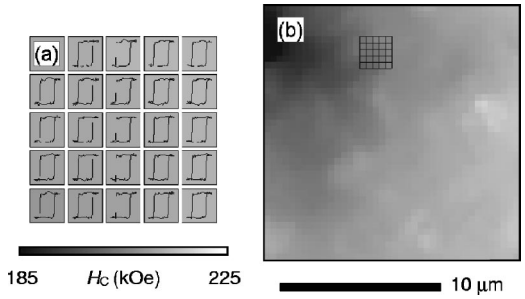

FIG. 6. (a) Typical hysteresis loops measured from each corresponding local region of 400×400 nm^2 on a (2.5 Å Co/11 Å Pd)$_5$ sample, where the x axis is an applied field ranging from -0.4 to 0.4 kOe and the y axis is the normalized Kerr angle. (b) Distribution map of the local coercivity generated from the simultaneous probing of the local hysteresis loops.

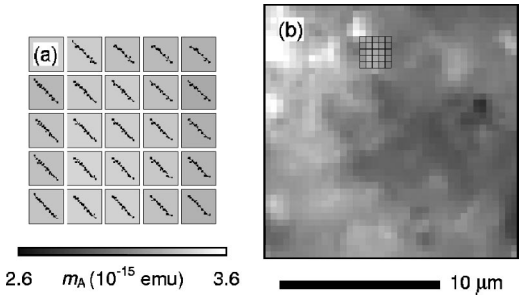

FIG. 8. (a) Typical field dependency measured from each corresponding local region shown in Fig. 6, where the x axis is an applied field ranging from 150 to 200 Oe and the y axis is the switching time on a logarithmic scale ranging from 1 to 100 s. The solid line in each box represents the best fit using Eq. (3). (b) Distribution map of the local activation magnetic moment generated from the simultaneous probing of the local field dependency.

tribution map from the local hysteresis loops by mapping the corresponding grays for each coercivity H_C onto the two-dimensional XY plane as shown in Fig. 6(b). The figure vividly shows the spatial fluctuation of the local coercivity on a submicrometer scale; the local areas having the lowest coercivity, indicated by black, are nucleation sites in the magnetization reversal process we describe later.

Another interesting application of the MOMM is to investigate the local dynamic behavior during magnetization reversal under a constant magnetic field.[11–13] The typical magnetization viscosity curves[40] are illustrated in Fig. 7(a), where each curve represents the local viscosity of each corresponding unit area of 400×400 nm^2. Each curve was averaged by 16 sequential measurements to reduce the error from the statistical reversal probability. In each curve, the x axis is the elapsed time after applying a reversing magnetic field on a logarithmic scale with a range from 0.2 to 20 s, and the y axis is the normalized Kerr signal. It is clearly seen from the curves that the magnetization viscosity curves change on a submicrometer scale. The switching time τ, required to reverse half the volume of each pixel was determined from each corresponding curve and the magnitude of the switching time is indicated by filling the corresponding grays on each pixel according to the gray palette at the bottom of the figure. Therefore using the MOMM we can generate the spatial distribution map of the local reversal time on a submicrometer scale from the viscosity curve measurement

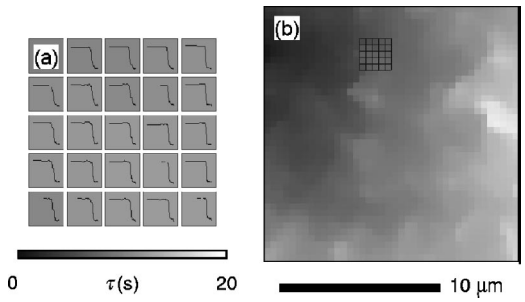

FIG. 7. (a) Typical viscosity curves measured from each corresponding local region shown in Fig. 6, where the x axis is the elapsed time on a logarithmic scale with a range from 0.2 to 20 s and the y axis is the normalized Kerr angle. The curves were obtained under a constant magnetic field of 196 Oe, which corresponded to an approximately 90% mean coercivity. (b) Distribution map of the local switching time generated from the simultaneous probing of the local viscosity curves.

as illustrated in Fig. 7(b). The figure clearly shows that the local reversal time is also nonuniform on a submicrometer scale. Domain reversal dynamics of this sample is dominated by the wall-motion process from several nucleation sites, located at the isolated black spots that show a faster reversal time. The smooth variation of the reversal-time distribution indicates a gradual expansion of domains via a continuous wall-motion process from the nucleation sites. The nonisotropic domain reversal behavior implies that there are spatial inhomogeneities in the magnetic properties, possibly caused by structural and/or chemical variation.

Crucial information about the dynamic properties was obtained from the magnetic field dependence of the switching time.[26] We measured an array of the field dependency of the local regions by tracing the switching time at every corresponding pixel under various applied magnetic fields. The field dependency of the switching time is illustrated in each box of Fig. 8(a), where the x axis is an applied magnetic field on a linear scale and the y axis is the switching time on a logarithmic scale. We clearly see from each box that the switching time depends exponentially on the applied magnetic field. The exponential dependency could be analyzed within a context of a thermally activated relaxation process:

$$\tau=\tau_0\exp[M_S V_A(H_C-h)/k_B T], \tag{3}$$

where τ_0 is the characteristic switching time for the coercivity H_C. The equation is derived from the Neél–Brown model[41,42] assuming a first-order uniaxial anisotropy by linear expansion of the energy barrier with h near the mean coercivity. The clear exponential dependency for every local region directly demonstrates that a thermally activated magnetization reversal process takes place, respectively, on the local regions on a submicrometer scale in ferromagnetic thin films. It is worthwhile to mention that we could determine the activation magnetic moment m_A $(=M_S V_A)$ from a best fit using Eq. (3). The activation magnetic moment essentially characterizes the basic magnetic moment acting as a single magnetic particle during magnetization reversal, but the physical interpretation of the activation magnetic moment is rather complicated since it is not only ascribed to the intrinsic local nature but is also affected by the interaction with the magnetization states of neighboring regions. However, it was confirmed that the activation magnetic moment was repro-

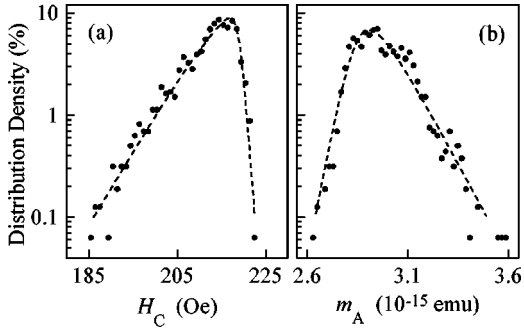

FIG. 9. (a) Distribution density of the local coercivity from the sample shown in Fig. 6, where the density was obtained for every 1 Oe interval. The solid line shows the best fit using a phenomological equation. (b) Distribution density of the local activation magnetic moment from the sample shown in Fig. 8, where the density was obtained for every 2×10^{-17} emu interval.

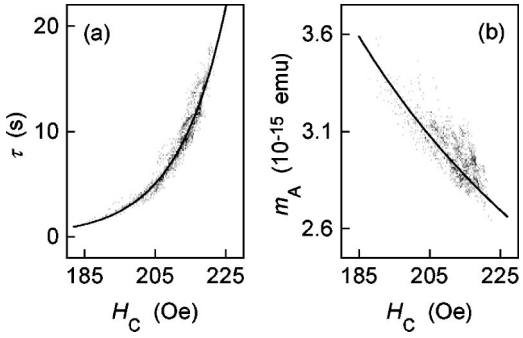

FIG. 10. (a) Correlated distribution between the coercivity H_C in Fig. 6 and switching time τ in Fig. 7. The solid line represents the best fit using Eq. (3). (b) Correlated distribution between the coercivity H_C in Fig. 6 and activation magnetic moment m_A in Fig. 8. The solid line guides an inverse proportionality.

duceable on any local region in a given sample. Figure 8(b) shows the local variation map of the activation magnetic moment.

B. Statistical distribution of local magnetic properties

The MOMM measurement provides a statistical treatment of the distribution of the local magnetic properties. In Fig. 9(a) we illustrate the distribution density of the local coercivity of the sample shown in Fig. 6. Interestingly, our experimental results directly show that the coercivity distribution is far from a Gaussian (or Lorentzian) distribution. The non-Gaussian distribution might come from the magnetic interaction between the nonisolated local regions in ferromagnetic thin films via the exchange and magnetostatic coupling, which results in a situation different from the case of isolated random phenomenon that would produce a Gaussian distribution. Also, it closely relates to the energy barrier distributions of the wall-pinning and nucleation processes during magnetization reversal. The asymmetric shape has already been considered in the Preisach approach, but the detailed shape of the distribution density was far from any well-known theoretical models, such as the lognormal-Gaussian and the factorized Lorentzian distributions:[38] Serious deviations were found for the two distribution models at either the low or high regimes, respectively. The distribution of the activation magnetic moment is also observed to be neither Gaussian nor Lorentzian, as seen in Fig. 9(b). To the best of our knowledge, this is the first time that the nonuniform distribution of the activation magnetic moment on a submicrometer scale has been probed.

C. Correlations between local magnetic properties

It is interesting to note that the switching time distribution in Fig. 7 is truly coincident with the coercivity distribution in Fig. 6. For a quantitative analysis of the correlation, we have measured the number of pixels $N(H_C,t)$ obtained by counting the pixels having the corresponding values of $H_C(x,y)$ and $\tau(x,y)$ measured at the same (x,y)th pixel in the map. Figure 10(a) illustrates the correlated distribution of $N(H_C,\tau)$ on a logarithmic scale in the $H_C-\tau$ coordinate. In the figure, we clearly see that the local switching time is truly correlated with the coercivity distribution. The correlated distribution is rather diffuse since the reversal dynamics is a statistical phenomena based on the reversal probability. It was experimentally confirmed that by averaging over a larger number of observations the reversal pattern approached a certain statistical ensemble. The correlation could be analyzed within the context of a thermally activated relaxation process. The solid line in Fig. 10(a) represents the best fit of the correlated distribution by fitting an exponential dependence to the thermally activated relaxation process as given by Eq. (3). An excellent theoretical correlation fitting with the experimental data provides strong evidence that the magnetization reversal in ferromagnetic thin films could be described by a thermally activated reversal process based on the local coercivity variation on a submicrometer scale.[25]

We also see a correlation between the activation magnetic moment and the coercivity. In Fig. 10(b), we illustrate the correlated distribution in the H_C-m_A coordinate. The figure shows that the activation magnetic moment inversely correlates with the coercivity, as shown by the best fit solid line. The inverse proportionality possibly comes from the contribution of the anisotropy field, which is known to be inversely proportional to the magnetization.

ACKNOWLEDGMENT

This work was supported by the Korean Ministry of Science and Technology through the Creative Research Initiative Project.

[1] J. L. Simonds, Phys. Today **48**, 26 (1995).
[2] K. M. Krishnan, MRS Bull. **20**, 24 (1995).
[3] G. A. Prinz, Science **282**, 1660 (1998).
[4] W. Bonet, W. Wernsdorfer, B. Barbara, A. Benoit, D. Mailly, and A. Thiaville, Phys. Rev. Lett. **83**, 4188 (1999).
[5] R. P. Cowburn, D. K. Koltsov, A. O. Adeyeye, and M. E. Welland, Appl. Phys. Lett. **73**, 3947 (1998); Phys. Rev. Lett. **81**, 5414 (1998).
[6] T. Aign, P. Meyer, S. Lemerle, J. P. Jamet, J. Ferré, V. Mathet, C. Chappert, J. Gierak, C. Vieu, F. Rousseaux, H. Launios, and H. Bernas, Phys. Rev. Lett. **81**, 5656 (1998).
[7] J.-P. Jamet, S. Lemerle, P. Meyer, J. Ferré, B. Bartenlian, N. Bardou, C. Chappert, P. Veiller, F. Rousseaux, D. Decanini, and H. Launois, Phys. Rev. B **57**, 14320 (1998).
[8] J. Ferré, J. P. Jamet, and P. Meyer, Phys. Status Solidi A **175**, 213 (1999).
[9] S.-B. Choe and S.-C. Shin, J. Appl. Phys. **85**, 5651 (1999).
[10] B. Raquet, R. Mamy, and J. C. Ousset, Phys. Rev. B **54**, 4128 (1996).

[11] J. Pommier, P. Meyer, G. Pónissard, J. Ferré, P. Bruno, and D. Renard, Phys. Rev. Lett. **65**, 2054 (1990).
[12] A. Kirilyuk, J. Ferré, V. Grolier, J. P. Jamet, and D. Renard, J. Magn. Magn. Mater. **171**, 45 (1997).
[13] S.-B. Choe and S.-C. Shin, Phys. Rev. B **57**, 1085 (1998).
[14] R. D. Kirby, J. X. Shen, R. J. Hardy, and D. J. Sellmyer, Phys. Rev. B **49**, 10810 (1994).
[15] A. Lyberatos, J. Earl, and R. W. Chantrell, Phys. Rev. B **53**, 5493 (1996).
[16] U. Nowak, J. Heimel, T. Kleinfeld, and D. Weller, Phys. Rev. B **56**, 8143 (1997).
[17] S.-B. Choe and S.-C. Shin, IEEE Trans. Magn. **36**, 3167 (2000).
[18] A. Lyberatos, J. Phys. D **33**, R117 (2000).
[19] J. X. Shen, R. D. Kirby, Z. S. Shan, D. J. Sellmyer, and T. Suzuki, J. Appl. Phys. **73**, 6418 (1993).
[20] A. Moschel, R. A. Hyman, and A. Zangwill, Phys. Rev. Lett. **77**, 3653 (1996).
[21] H.-P. D. Shieh and M. H. Kryder, IEEE Trans. Magn. **24**, 2464 (1988).
[22] M. Speckmann, H. P. Oepen, and H. Ibach, Phys. Rev. Lett. **75**, 2035 (1995).
[23] J. Ferré, V. Grolier, P. Meyer, S. Lemerle, A. Maziewski, E. Stefanowicz, S. V. Tarasenko, V. V. Tarasenko, M. Kisielewski, and D. Renard, Phys. Rev. B **55**, 15092 (1997).
[24] H. Hopster, Phys. Rev. Lett. **83**, 1227 (1999).
[25] S.-B. Choe and S.-C. Shin, Phys. Rev. B **62**, 8646 (2000).
[26] S.-B. Choe and S.-C. Shin, Appl. Phys. Lett. **78**, 1430 (2001).
[27] S.-B. Choe and S.-C. Shin, J. Appl. Phys. **87**, 6848 (2000).
[28] E. Dan Dahlberg and J.-G. Zhu, Phys. Today **48**, 34 (1995).
[29] E. Betzig, J. K. Trautman, R. Wolfe, E. M. Gyorgy, P. L. Finn, M. H. Kryder, and C. H. Chang, Appl. Phys. Lett. **61**, 142 (1992).
[30] M. R. Scheinfein, J. Unguris, M. H. Kelley, D. T. Pierce, and R. J. Celotta, Rev. Sci. Instrum. **61**, 2501 (1990).
[31] R. Wiesendanger, H.-J. Güntherodt, G. Güntherodt, R. J. Gambino, and R. Ruf, Phys. Rev. Lett. **65**, 247 (1990).
[32] H. Poppa, E. Bauer, and H. Pinkvos, MRS Bull. **20**, 38 (1995).
[33] S. Anders, H. A. Padmore, R. M. Duarte, T. Renner, M. R. Scheindein, J. Stöhr, L. Séve, and B. Sinkovic, Rev. Sci. Instrum. **70**, 3973 (1999).
[34] P. Fischer, T. Eimüller, G. Schütz, P. Guttmann, G. Schmahl, K. Prügl, and G. Bayreuther, J. Phys. D **31**, 649 (1998).
[35] S.-B. Choe and S.-C. Shin, Phys. Rev. B **86**, 532 (2001).
[36] H.-P. D. Shieh and M. H. Kryder, J. Appl. Phys. **61**, 1108 (1987).
[37] B. E. Bernacki and M. Mansuripur, J. Appl. Phys. **69**, 4960 (1991).
[38] G. Bertotti, *Hysteresis in Magnetism* (Academic, San Diego, 1998), Part IV.
[39] M. Mansuripur, *The Physical Principles of Magneto-Optical Recording* (Cambridge University Press, Cambridge, England, 1995), Chap. 15.
[40] M. Labrune, S. Andrieu, F. Rio, and P. Bernstein, J. Magn. Magn. Mater. **80**, 211 (1989).
[41] L. Neél, Ann. Geophys. (C.N.R.S.) **5**, 99 (1949).
[42] W. F. Brown, Phys. Rev. **130**, 1677 (1963).